



RESEARCH ARTICLE | SEPTEMBER 24 2024

Flexible non-Brownian filament in intensified shear flow

Yetao Lu (卢叶涛); Haibo Huang (黄海波)  



Physics of Fluids 36, 093347 (2024)

<https://doi.org/10.1063/5.0230485>



Articles You May Be Interested In

A vortex flow intensified by thermal convection

Physics of Fluids (January 2017)

Intensifying interfacial oscillations in falling film flows over rectangular corrugations

Physics of Fluids (September 2024)

Delayed yield in colloidal gels: Creep, flow, and re-entrant solid regimes

J. Rheol. (July 2016)



Physics of Fluids

Special Topics Open for Submissions

[Learn More](#)



Flexible non-Brownian filament in intensified shear flow

Cite as: Phys. Fluids **36**, 093347 (2024); doi: [10.1063/5.0230485](https://doi.org/10.1063/5.0230485)

Submitted: 24 July 2024 · Accepted: 5 September 2024 ·

Published Online: 24 September 2024



View Online



Export Citation



CrossMark

Yetao Lu (卢叶涛) and Haibo Huang (黄海波)^{a)} 

AFFILIATIONS

Department of Modern Mechanics, University of Science and Technology of China, Hefei, Anhui 230026, China

^{a)} Author to whom correspondence should be addressed: huanghb@ustc.edu.cn

ABSTRACT

The behavior of a three-dimensional, non-Brownian flexible filament in a low Reynolds number shear flow was investigated through theoretical and numerical analyses. In the phase plane with Reynolds number $Re \in [0.03, 8]$ and flow intensity $Z \in [800, 35\,000]$, four primary motion modes of the filament were identified: rigid, C-buckling, U-turn, and S-turn. By employing the principle of symmetry, a theoretical model was developed to explain the S-turn mode, and we discovered that the critical flow strength for the transition from U-turn to S-turn was approximately $Z_c = 4900$. Our numerical simulations confirmed this transition value. In a system devoid of thermal fluctuations, it was observed that the mode transitions of microscale filament precisely corresponded to the abrupt scale rate changes in the non-Newtonian behavior of the macroscopic solution. Although the polymer stress under different modes has distinct underlying causes, they can all be predicted by the generalized Hooke's law.

Published under an exclusive license by AIP Publishing. <https://doi.org/10.1063/5.0230485>

I. INTRODUCTION

Interaction between slender bodies and fluids is a common occurrence in nature. Bearded cats and catfish use their whiskers to detect small perturbations.¹ Flagella are used by bacteria and sperm for movement in viscous flow,² while the cytoskeleton controls the position of subcellular structures, such as nuclei, chromosomes, and organelles, in eukaryotic cells.³ The helix and folding of DNA are subject to thermal fluctuations,⁴ and cellulose filaments collide and join due to fluid driving forces.⁵ Despite the simple appearance of filaments, they exhibit a wealth of physical phenomena. This is attributed to the larger spatial scale of flexible filaments in one direction, leading to many degrees of freedom for deformation and the possibility of unstable buckling with a characteristic time much smaller than that of tumbling and migration. Hence, the multi-scale effects in both space and time make it a fascinating field to investigate.

The dynamics of a rigid filament immersed in a shear flow has been extensively studied. Jeffery⁶ investigated the behavior of rigid ellipsoidal particles and demonstrated that, in a shear flow, these particles undergo continuous tumbling along a Jeffery orbit without decay. Cox⁷ proposed an empirical formula of equivalent aspect ratio $r_e = 1.24r_p/\sqrt{\ln r_p}$ to extend Jeffery's orbit to cylinders, e.g., filaments, where r_p is the aspect ratio of the filament (the ratio of length to diameter). In the presence of inertial forces, the filament drifts toward the shearing plane at the rate of $O(Re)$ when the

Reynolds number (Re) is small.⁸ When Re is above a critical value, i.e., Re_c , the filament stops tumbling completely.⁹ At a finite Re and $Re < Re_c$, the rotation period is proportional to $(Re_c - Re)^{-1/2}$.¹⁰ The above conclusion is quantitatively applicable to the cases of flexible filaments.¹¹

The deformation of flexible filaments when immersed in a shear flow is a highly complex phenomenon.¹² As reported by Salinas and Pittman,¹³ these filaments undergo a series of morphological transitions as the shear rate is increased, as seen in Fig. 5. In an experiment involving nylon filaments in corn syrup, Forgacs and Mason¹⁴ observed C-buckling [Fig. 5(b)]. However, the theoretical prediction of the critical flow strength differed from the experimental observation by about a factor of 2. To address this gap between theory and experiment, Becker and Shelley¹⁵ used the pseudo-spectral collocation method and correctly predicted the critical flow strength of C-buckling. Building on these studies, Harasim *et al.*¹⁶ proposed a theoretical model for the U-turn mode [Fig. 5(c)], using the analogy of comparing flexible filaments with flexible capsules. However, Liu *et al.*¹⁷ noted that the straight portion of the filament is not always aligned with the direction of flow but has a specific angle of inclination. This new insight allowed the researchers to obtain a critical flow strength for the morphological transition from C-buckling to the U-turn. As the flow strength increases, the flexible filament undergoes morphological transition from U-turn to S-turn [Fig. 5(d)], which is

the primary focus of this paper. Theoretical prediction of this specific transition is not available in the literature, as far as we know.

The filament suspension may exhibit elastic behavior.¹⁸ The behavior can be quantified through the measurement of normal stresses. Typically, the first normal stress N_1 is assumed to be in the direction of the flow line and accounts for phenomena such as rod-climbing and co-extrusion instability.^{19,20} The second normal stress N_2 is taken to be along the vortex line, accounting for phenomena like negative rod-climbing and bowing of the interface in the Tanner tilted channel.²¹ Goto and Nagazono¹⁸ studied dilute solutions containing flexible filaments and experimentally found that if the shear rate exceeded a critical value, the normal stress underwent an abrupt transition from zero to positive. Becker and Shelley¹⁵ numerically simulated non-Brownian flexible filaments and showed that this critical shear rate corresponded exactly to the onset of C-buckling. Chakrabarti *et al.*²² investigated the three-dimensional rheological properties of Brownian filaments and found that the morphological transition from C-buckling to U-turn corresponds to a change in the scale law of rheological properties. However, this study does not explicitly establish a detailed connection between the deformation characteristics of the filament and the non-rheological properties of the solution.

It was discovered that there is a definite connection between the tensor $\mathbf{n}^{(p)}$ of optical anisotropy or birefringence of theta solutions and the polymer stress tensor $\Sigma_{xx}^{(p)}$.²³ This proportionality $\mathbf{n}^{(p)} = C\Sigma_{xx}^{(p)}$ is called the stress-optic law,²⁴ where C is a constant that depends on temperature.^{25,26} From a reductionist perspective, both the optical anisotropy and the polymer stress share a common cause, which is the deformation and orientation of the filament. Once this connection is established, we will be able to *a priori* predict the complex non-Newtonian behavior of macroscopic solutions based solely on knowledge of the microscopic properties of the filaments. In this regard, previous studies have focused extensively on Gaussian chains, but there have been relatively few studies on non-Brownian fibers.

In this study, we employ a combined theoretical and numerical approach to investigate the behavior of non-Brownian filaments in three-dimensional Couette flow, with a particular focus on analyzing the microscopic morphological changes from U-turn to S-turn and the corresponding macroscopic rheological properties. The remaining sections of the paper are structured as follows: Sec. II describes the physical problems and numerical method used in our investigation, while Sec. III presents the theoretical model of the U-turn to S-turn transition and provides a detailed discussion. Finally, our concluding remarks are presented in Sec. IV.

II. PHYSICAL PROBLEM AND COMPUTATIONAL MODEL

A. Physical problem

As shown in Fig. 1(a), the dynamics of a flexible non-Brownian filament immersed in shear flow is controlled by the interplay of inertial, viscous, and elastic forces. The forces can be represented using two non-dimensional parameters, the Reynolds number (Re), and flow strength (Z). The Reynolds number is defined by $Re = \rho\dot{\gamma}L^2/\mu$, which represents the ratio of inertial force to viscous force in the fluid. Here, ρ is the fluid density, $\dot{\gamma}$ is the shear rate, L is the length of filament, and μ is the dynamic viscosity. Flow strength, defined as $Z = \dot{\gamma}\tau_r/c$, represents the ratio between the hydrodynamic force generated by viscosity and the restoring force generated by the elasticity of the filaments. The characteristic relaxation time of bending deformations $\tau_r = 8\pi\mu L^4/B$,

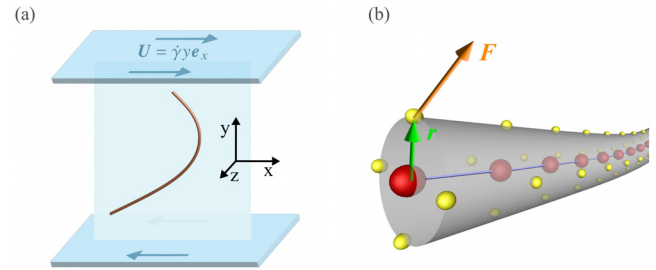


FIG. 1. (a) Flexible filaments deform in Couette flow. (b) Perspective view of the filament. The large red circles represent finite element nodes, the blue solid lines denote finite element elements, and the yellow spheres indicate ghost points.

where B represents the bending stiffness. The asymptotic geometric parameter, $c = -\ln(\varepsilon^2 e)$, emerges from the local mobility operator,²⁷ where $\varepsilon = d/L$ is the inverse aspect ratio and d is the diameter of the filament. In this article, ε is fixed to be $\frac{1}{64}$.

We investigate flows where the fluid displays nearly incompressible behavior. The governing equations for the flow field are the Navier–Stokes (N–S) equations,

$$\frac{\partial \mathbf{u}}{\partial t} + \nabla \cdot (\mathbf{u} \otimes \mathbf{u}) = -\nabla p + \frac{1}{Re} \nabla^2 \mathbf{u} + \mathbf{f}, \quad (1)$$

$$\nabla \cdot \mathbf{u} = 0,$$

where \mathbf{u} is the velocity, p is the pressure, and \mathbf{f} is the external volume force.

In the present work, the solid part is a slender body, which can be described by the Euler–Bernoulli beam model with large deformation. The neutrally buoyant filament is described in a Lagrangian coordinate system and the structure equation is employed,^{28,29}

$$\left(\frac{\rho_f/A_f - \rho}{\rho} \right) \frac{\partial^2 \mathbf{X}}{\partial t^2} = \frac{\partial}{\partial s} \left[S \left(1 - \left(\frac{\partial \mathbf{X}}{\partial s} \cdot \frac{\partial \mathbf{X}}{\partial s} \right)^{-1/2} \right) \frac{\partial \mathbf{X}}{\partial s} - \frac{\partial}{\partial s} \left(B \frac{\partial^2 \mathbf{X}}{\partial s^2} - \mathbf{M}^s \right) \right] + \mathbf{F}^s, \quad (2)$$

where \mathbf{X} is the position, s the curvilinear coordinate along the filaments centerline, ρ_f the filament linear density, and $A_f = \frac{1}{4}\pi d^2$ the cross sectional area. A very large tensile stiffness of $S = 1000$ is adopted in order to approximate axial non-tensile conditions. The bending rigidity $B = EI$, where E is Young’s modulus and $I = A_f \frac{d^2}{16}$ is the second moment of area. The fluid force acting on the filament segment is denoted by \mathbf{F}^s and the torque acting on the filament segment is denoted by \mathbf{M}^s . The reason why Eq. (2) can be used to describe a filament with an finite aspect ratio of 64 is that for all the examples discussed here, the radius of curvature of the axis of the filament is always much larger than the radius of the filament. For slender bodies, this means that even though the overall geometrical deformation is large, the strain is still small. Such physical problems themselves guarantee the validity of Eq. (2). The boundary conditions of the filament at both ends are

$$1 - \left(\frac{\partial \mathbf{X}}{\partial s} \cdot \frac{\partial \mathbf{X}}{\partial s} \right)^{-1/2} = 0, \quad \frac{\partial^2 \mathbf{X}}{\partial s^2} = (0, 0), \quad \frac{\partial^3 \mathbf{X}}{\partial s^3} = (0, 0), \quad (3)$$

which mean no tension force, no bending moment and no shearing force, respectively.

The filament is initially placed along the streamline. A small initial deformation $\sum_{n=2}^{10} a_n \Phi_n$ with $a_n = 0.01/(n+1)^4$ and $\Phi_n = (s^2 - 1/4)T_n(2/s)$ is applied to the filament, which is similar to that presented in the work of Becker and Shelley,¹⁵ where $T_n(s)$ is a Chebyshev polynomial, and the origin of s is located at the midpoint of the filament. The filament is then automatically aligned with velocity-gradient plane motion and undergoes deformation within the plane. The formulations described above are normalized using reference quantities, such as fluid density ρ , filament length L , and time $\dot{\gamma}^{-1}$.

B. Numerical method

The incompressible N-S equation is solved by the MRT lattice Boltzmann method.³⁰ The evolution equation is

$$f_i(\mathbf{x} + \mathbf{e}_i \Delta t, t + \Delta t) - f_i(\mathbf{x}, t) = -\mathbf{M}^{-1} \mathbf{S} \mathbf{M} [f_i(\mathbf{x}, t) - f_i^{\text{eq}}(\mathbf{x}, t)] \Delta t + F_i \Delta t, \quad (4)$$

where $f_i(\mathbf{x}, t)$ is the distribution function for velocity \mathbf{e}_i at position \mathbf{x} and time t , F_i is the forcing term, \mathbf{M} the transformation matrix, and \mathbf{S} the relaxation matrix. The macroscopic variables can be calculated from

$$\rho = \sum_i f_i, \quad \rho \mathbf{u} = \sum_i \mathbf{e}_i f_i + \frac{1}{2} \mathbf{f} \Delta t, \quad p = c_s^2 \rho. \quad (5)$$

The structure equation is discretized by a nonlinear finite element method with co-rotational scheme.²⁸ The fluid–solid interaction is coupled through the immersed boundary method (IBM).^{31,32} In the IBM, the fluid force acting on the Lagrangian point, i.e., \mathbf{F} , is spread to surrounding Euler points (fluid nodes) by delta function to make sure the no-slip boundary condition is satisfied. To assess the torque exerted by the fluid on the filament, four orthogonal ghost points are placed around each solid Lagrangian point, as depicted in Fig. 1(b). The green arrow represents \mathbf{r} , which signifies the position vector from the Lagrangian point to the respective ghost points, and $|\mathbf{r}| = \varepsilon/2$. The orange arrow represents \mathbf{F} , denoting the forces calculated using the Immersed Boundary (IB) method at these ghost points. The external force and torque at the internal finite element i th nodes are given by

$$\mathbf{F}_i^s = \sum_{j=1}^4 \mathbf{F}_{ij}, \quad (6)$$

$$\mathbf{M}_i^s = \sum_{j=1}^4 \mathbf{r}_{ij} \times \mathbf{F}_{ij} \quad \text{on } i \neq 1, (i) \text{max}.$$

Subscript i represents the finite element node number, and subscript j represents the ghost point number. For example, \mathbf{r}_{ij} refers to the vector that points from the i th finite element node to its corresponding j th ghost point. Here, \mathbf{F}_{ij} can be calculated by the penalty scheme,³³

$$\mathbf{F}_{ij} = \alpha \int_0^t [\mathbf{V}^f(\mathbf{X}_{ij}, t') - \mathbf{V}^s(\mathbf{X}_{ij}, t')] dt' + \beta [\mathbf{V}^f(\mathbf{X}_{ij}, t) - \mathbf{V}^s(\mathbf{X}_{ij}, t)], \quad (7)$$

where α and β are parameters selected based on previous studies.¹¹ $\mathbf{V}^s(\mathbf{X}_{ij}, t) = \frac{\partial \mathbf{X}_{ij}}{\partial t}$ is the velocity of the filament at the ghost points and

\mathbf{V}_f is the fluid velocity at the position \mathbf{X}_{ij} obtained by interpolation. The interpolation function can be written as

$$\mathbf{V}^f(\mathbf{X}_{ij}, t) = \int_{\Omega} \mathbf{v}(\mathbf{x}, t) \delta(\mathbf{x} - \mathbf{X}_{ij}) d\mathbf{x}, \quad (8)$$

where δ is the Dirac delta function and the subscript Ω denotes the whole computational domain. Subsequently, the volume force on the Euler grid (the force acting on fluid points) can be obtained,

$$\mathbf{f}(\mathbf{x}, t) = - \int_{\Gamma} \mathbf{F}(\mathbf{X}_{ij}, t) \delta(\mathbf{x} - \mathbf{X}_{ij}) ds. \quad (9)$$

To avoid the issue of pseudo-oscillation associated with the weak fluid–structure coupling problem, we have adopted a C^2 continuous delta function,³⁴

$$\delta(r) = \begin{cases} \frac{3}{8} + \frac{\pi}{32} - \frac{r^2}{4}, & |r| \leq 0.5, \\ \frac{1}{4} + \frac{1-|r|}{8} \sqrt{-2+8|r|-4r^2} - \frac{1}{8} \arcsin(\sqrt{2}(|r|-1)), & 0.5 \leq |r| \leq 1.5, \\ \frac{17}{16} - \frac{\pi}{64} - \frac{3|r|}{4} + \frac{r^2}{8} + \frac{|r|-2}{16} \sqrt{-14+16|r|-4r^2} + \frac{1}{16} \arcsin(\sqrt{2}(|r|-2)), & 1.5 \leq |r| \leq 2.5, \\ 0, & 2.5 \leq |r|. \end{cases} \quad (10)$$

The persistent pseudo-oscillation problem, prevalent due to the small linear density ratio of the filament, is thereby tackled. In order to obtain accurate and stable solutions, we have introduced predictors to determine the provisional velocity and position of the fluid–structure interface at each time step.³⁵

To maintain the condition of zero torque at both ends of the filament, the torque at the free end nodes should be set as $\mathbf{M}_i^s = -\sum_{j=1}^4 \mathbf{r}_{ij} \times \mathbf{F}_{ij}$ on $i = 1, (i) \text{max}$.²⁹ Although torque is a small quantity [$O(\varepsilon^2)$] for slender filaments, when the filament’s orientation lies in the zero-velocity plane, this torque becomes the sole driving factor for filament rotation. Therefore, accurately assessing torque is crucial.

C. Validation and verification

To validate our numerical method, we simulated several typical cases. First, the simulation of a rope pendulum in a vacuum with $B = 0.01$ and $Fr = gL/U_{ref}^2 = 10$ was performed. As depicted in Fig. 2(a), the rope is initially released from the left end in a stationary state, and it swings to the right under the influence of gravity alone. In this case, we adopted a spatial resolution of $\Delta s = 1/64$ to discretize the rope, and two temporal resolutions were implemented: $\Delta t = T/32$ and $\Delta t = T/160$, where T denotes the period of the rope’s pendulum-like oscillation. Figure 2(b) illustrates the y -direction displacement of the rope’s free end under varying temporal resolutions, and the result of Huang *et al.*³⁶ is also presented for comparison. The results obtained

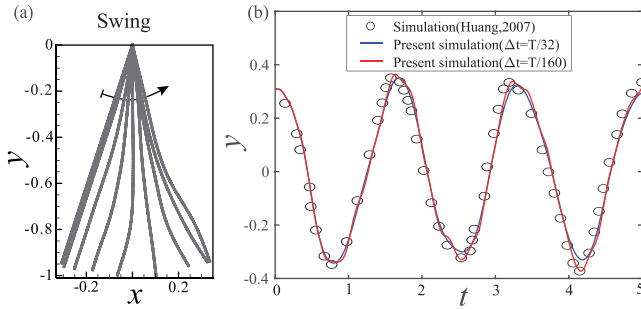


FIG. 2. (a) The rope swings under the influence of gravity. (b) End displacement of rope swing in vacuum.

from both temporal resolutions align harmoniously with those of Huang *et al.*,³⁶ despite the presence of marginal numerical dissipation when $\Delta t = T/32$.

Second, we simulated the cases of a rigid filament tumbling in shear flow at $Re = 0.1$. In this case, the spatial resolution is also set at $\Delta s = 1/64$, with a time resolution of $\Delta t = 2 \times 10^{-4}$. As shown in Fig. 3(a), the rigid filament is initially aligned with the flow direction and subsequently undergoes periodic tumbling within the velocity-gradient plane due to fluid motion. Figure 3(b) shows that our results agree well with the numerical, experimental, and theoretical data^{7,31,37} for the non-dimensional tumbling period T_p as a function of r_p .

Finally, we tested the flexural deformation of a flexible filament in shear flow,^{14,31} as sketched in Fig. 4(a). To replicate the experimental

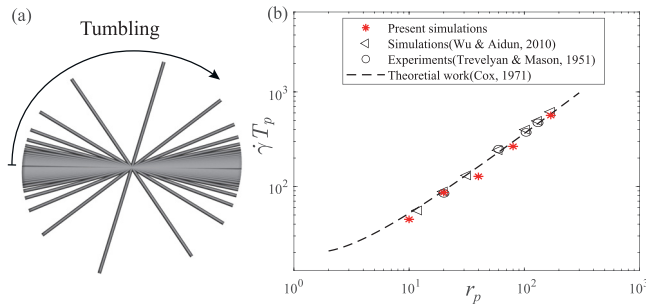


FIG. 3. (a) Rigid filament tumbling in shear flow (plotted at equal time intervals) and (b) tumbling period of a rigid filament in shear flow.

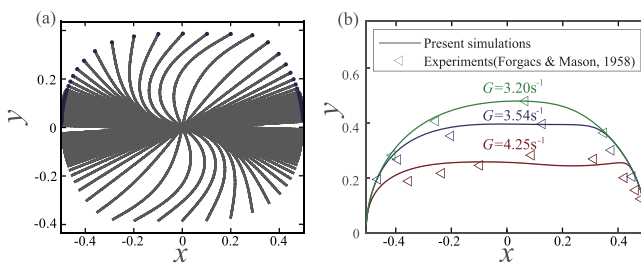


FIG. 4. (a) Flexible filament undergoes deformation in shear flow at dimensional shear rate of $G = 3.54 \text{ s}^{-1}$ (plotted at equal time intervals), (b) the end position of the filament undergoing deformation in shear flows with different dimensional shear rates: $G = 3.20, 3.54, \text{ and } 4.25 \text{ s}^{-1}$.

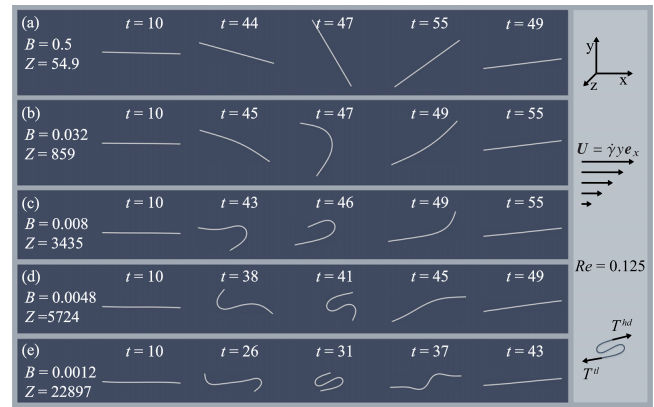


FIG. 5. Our numerical result for typical morphological evolutions of filament over a half-period: (a) Rigid motion, (b) C-buckling motion, (c) U-turn motion, (d) and (e) S-turn motion. Multimedia available online.

results, we set the parameters identical to those in the experiment of Forgacs and Mason:¹⁴ the filament diameter $d = 0.0122 \text{ mm}$, aspect ratio $r_p = 170$, dimensional Young's modulus $E_Y = 6.3 \text{ GPa}$, and dynamic viscosity $= 9.12 \text{ Pas}$. In the simulations, the computational domain size is $5L \times 5L \times 3L$, which is large enough to eliminate the boundary effect. Our grid-independence study showed that $\Delta x = \Delta y = \Delta z = \frac{1}{100}$ and $\Delta s = \frac{1}{64}$ were sufficient to obtain accurate results. Figure 4(b) shows the displacement of the filament's end, which is consistent with experimental data.¹⁴ Additionally, our three-dimensional numerical method for fluid-structure interactions was validated in Zhang *et al.*³⁸

III. RESULTS AND DISCUSSION

Figure 5 (Multimedia view) displays the results of our numerical experiments. The settings of computational domain and mesh size in these simulations are consistent with those used in the last validation case. Under the condition of $Re = 0.125$ and $r_p = 64$, we obtained four typical modes of motion under different flow strengths. This mode classification is not new; it just provides readers with a visual understanding. As discussed in Sec. I, most of the related work has been focused on conditions with low flow strength. The transition from U-turn to S-turn, though complex and intriguing, has never been extensively explored.

A. Theoretical model of S-turn

One possible theoretical method for analyzing the motion mode of the filament is to assume a typical configuration at a critical time.^{16,17} The relative velocities between the filament and the background fluid can then be approximated to calculate the fluid-structure coupling forces. Through the force equilibrium equation for the filament, this problem can be completely solved. To determine this typical configuration, we look at the U-turn and S-turn modes, we find that they diverge at the moment when the deformation begins. If the initial deformation is asymmetric, as shown in Fig. 5(c) $t = 43$, that is, only one end is rolled up, then the filament will inevitably develop into a U-turn. In contrast, if the initial deformation is with both ends of the central symmetry rolled up at the same time, as shown in Fig. 5(e) $t = 26$, then the filament will develop an S-turn mode. We assume

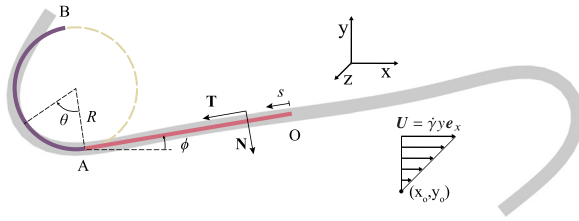


FIG. 6. S-turn configuration model. Bent part is approximated by semi-circle of radius R . Straight part has tilt angle ϕ and length l . Here, s represents arc length.

that the S-turn mode is highly symmetric, as depicted in Fig. 6. This assumption enables us to analyze only one half of it, comprising a semi-arc and a straight line. Notations “ \parallel ” and “ \perp ” are used to denote tangential and perpendicular components, respectively. Following are the expressions for the two components of the relative velocities of the AO segment:

$$v_{\parallel}^{rel}(s) = -\dot{\gamma}s \sin \phi \cos \phi, \quad v_{\perp}^{rel}(s) = v_{\perp}^{AO}(s) + \dot{\gamma}s \sin^2 \phi. \quad (11)$$

In our analysis, we utilized the resistive force theory proposed by Gray and Hancock,³⁹ in which the resistive force is assumed to be directly proportional to the relative velocity of the object, i.e.,

$$f_{\parallel} = c_{\parallel} v_{\parallel}^{rel}, \quad f_{\perp} = c_{\perp} v_{\perp}^{rel}, \quad (12)$$

where the coefficients $c_{\parallel} \approx 2\pi\mu/\ln(2L/d)$ and $c_{\perp} = 2c_{\parallel}$.¹⁷ Since there is no force perpendicular to the straight section AO, i.e., $f_{\perp} = 0$, through (11) we have

$$v_{\perp}^{AO}(s) = -\dot{\gamma}s \sin^2 \phi. \quad (13)$$

Similarly, the relative velocity of the arc part AB can be written as

$$v_{\parallel}^{rel}(\theta) = v_{\parallel}^{AB}(\theta) + v_f \cos(\theta - \phi), \quad (14)$$

$$v_{\perp}^{rel}(\theta) = v_{\perp}^{AB}(\theta) + v_f \sin(\theta - \phi), \quad (15)$$

where the background fluid velocity (without filament) $v_f = \dot{\gamma}R[\cos \phi - \cos(\theta - \phi)] - \dot{\gamma}l \sin \phi$, and all the elements on the arc must satisfy the force equilibrium condition such that

$$-\frac{1}{R} \frac{df_N}{d\theta} = c_{\parallel} v_{\parallel}^{rel}, \quad \frac{f_N}{R} + \frac{B}{R^3} = c_{\perp} v_{\perp}^{rel}. \quad (16)$$

Here, f_N is the axial internal force. Because the filament cannot be stretched, we have

$$\frac{dv_{\parallel}^{AB}}{d\theta} + v_{\perp}^{AB} = 0. \quad (17)$$

Substituting (14) into (17), we have

$$\frac{dv_{\parallel}^{rel}}{d\theta} - \frac{dv_f \cos(\theta - \phi)}{d\theta} + v_{\perp}^{AB} = 0. \quad (18)$$

Substituting the first formula in (16) into (18), we get

$$-2 \frac{d^2 v_{\perp}^{rel}}{d\theta^2} - \frac{dv_f \cos(\theta - \phi)}{d\theta} + v_{\perp}^{AB} = 0. \quad (19)$$

Further substituting (15) into (19), we get a second-order differential equation for v_{\perp}^{AB} ,

$$2 \frac{d^2 v_{\perp}^{AB}}{d\theta^2} - v_{\perp}^{AB} = -2 \frac{dv_f \sin(\theta - \phi)}{d\theta^2} - \frac{dv_f \cos(\theta - \phi)}{d\theta}. \quad (20)$$

According to the perpendicular velocity continuity condition at point A,

$$v_{\perp}^{AB}(0) = -\dot{\gamma}l \sin^2 \phi, \quad (21)$$

and the tension-free condition at point B,

$$v_{\perp}^{AB}(\pi) = \frac{B}{c_{\perp} R^3} + \dot{\gamma}(l \sin \phi - 2R \cos \phi) \sin \phi, \quad (22)$$

we have

$$v_{\perp}^{AB}(\theta) = C_1 \cosh(\lambda\theta) + C_2 \sinh(\lambda\theta) + \sum_{n=1,2} [\alpha_n \cos(n\theta) + \beta_n \sin(n\theta)], \quad (23)$$

where $\lambda = 1/\sqrt{2}$, and

$$C_1 = \frac{\dot{\gamma}R \sin(2\phi)}{18},$$

$$C_2 = \frac{B \operatorname{csch}(\lambda\pi)}{c_{\perp} R^3} - \frac{\dot{\gamma}R}{18} \sin(2\phi) \tanh\left(\frac{\lambda\pi}{2}\right), \quad (24)$$

$$\alpha_1 = -\dot{\gamma}(l \sin \phi - R \cos \phi) \sin \phi, \quad \alpha_2 = -\frac{5}{9} \dot{\gamma}R \sin(2\phi),$$

$$\beta_1 = +\dot{\gamma}(l \sin \phi - R \cos \phi) \cos \phi, \quad \beta_2 = \frac{5}{9} \dot{\gamma}R \cos(2\phi).$$

Then, we can naturally get the tangential velocity,

$$v_{\parallel}^{AB} = -v_{\parallel}^f - 2 \left(\frac{dv_{\perp}^{AB}}{d\theta} + \frac{dv_{\perp}^f}{d\theta} \right). \quad (25)$$

From the tangential velocity continuity condition and torque equilibrium condition at point A, we get

$$\frac{B}{18\mu R^5} \left[-14\mu R^4 \sin^2(\phi) + 9\pi\mu R^4 \sin(2\phi) + 14\mu R^4 \cos^2(\phi) + 18\mu R^4 + \sqrt{2}\mu R^4 \operatorname{csch}\left(\frac{\pi}{\sqrt{2}}\right) \sin(2\phi) - \mu R^3 \left(2\sqrt{2}R \coth\left(\frac{\pi}{\sqrt{2}}\right) + 9 \right) \sin(\phi) \cos(\phi) - 18\sqrt{2}\varepsilon \tanh\left(\frac{\pi}{2\sqrt{2}}\right) - 18\sqrt{2}\varepsilon \coth\left(\frac{\pi}{2\sqrt{2}}\right) \right] = 0, \quad (26)$$

and

$$M_A^{AB} = c_{\perp} R \int_0^{\pi} \cos^2\left(\frac{\theta}{2}\right) \left(v_{\parallel}^{AB} + v_f \cos(\theta - \phi) \right) - \sin \theta \left(v_{\perp}^{AB} + v_f \sin(\theta - \phi) \right) d\theta = \frac{2B}{R^2}, \quad (27)$$

respectively. The two equations above involve two unknowns, ϕ and R . It seems that the two unknowns can be determined. However, Eq. (27) is useless because according to the moment free condition of the

right side of point A, bending rigidity $B = 0$ or radius $R = \infty$ has to be satisfied. The underlying reason is that our model is only C^0 continuous at the point A, so boundary layer effects will emerge near it. Therefore, we are trying to find another equation in terms of conservation of energy. The basic idea is that as the shape of the filament evolves, a portion of the straight filament will be bent at the rate of V_{snake} , and the increased bending energy will equal the work done by the fluid,¹⁷ i.e.,

$$\dot{E} = B \int_0^L r_t \cdot r_{ssss} ds = \frac{BV_{snake}}{2R^2} = \int_0^L r_t \cdot F ds. \quad (28)$$

Here, the subscripts “t” and “s” denote derivatives with respect to t and s , respectively. The velocity at the end of the filament $|v_B|$ is chosen to approximate V_{snake} also due to the discontinuous derivative at point A. In this way, the problem is finally solved. Equations (26) and (28) only contain the unknowns ϕ and R . The emergence of at least one solution represents a transition between U-turn and S-turn.

Although our derivation drew inspiration from Liu *et al.*,¹⁷ our work differs significantly from theirs, as the main focus is placed on the S-turn, which possesses symmetry. While (Ref. 17) have primarily focused on the transition from Rigid to C-buckling or the transition from C-buckling to U-turn. These investigations primarily explore the phenomenon of spontaneous symmetry breaking,⁴⁰ resulting from the intensification of flow strength. In contrast, our study places considerable emphasis on the transition from U-turn to S-turn, which implies that flow strength exceeding a critical value triggers spontaneous symmetry restoration. Symmetry restoration is a pervasive phenomenon in nature. For instance, the presence of a strong magnetic field can restore electroweak symmetries,⁴¹ while chiral symmetry restoration has been observed at high matter density in pionic atoms.⁴²

B. Transitions between U-turn and S-turn

Transition criterion between U-turn and S-turn would be further discussed here. The transition occurs as the two curves represented by Eqs. (26) and (28) intersect in the ϕ - R plane. The two curves are shown in Fig. 7(a) and the intersection occurs approximately at $Z = 4900$. In other words, the critical flow strength for the transition is about $Z_c = 4900$.

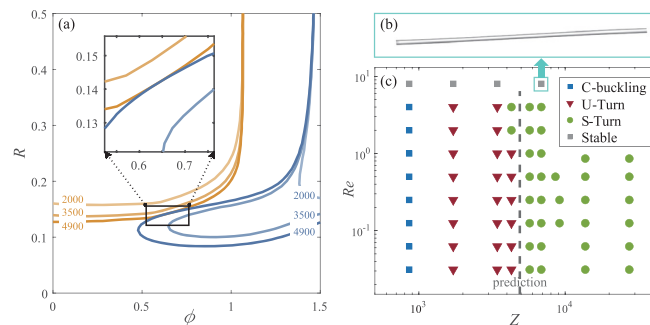


FIG. 7. (a) On the ϕ - R plane, the solid yellow and blue lines represent Eqs. (26) and (28), respectively. (b) The deformation of stable mode when $Re = 8$ and $Z = 6869$. (c) Phase diagrams, each symbol in the phase diagram denotes a simulated case.

Actually at $Z \approx Z_c$, U-turn and S-turn may be difficult to distinguish [see Fig. 5(d)]. A quantitative standard should be proposed. Here, we introduce the dot product of the normal vector of the two transverse planes $\langle T^{hd}, T^{tl} \rangle$ (as shown in the lower right corner of Fig. 5). The basic idea is as follows: at some moment in a period, the two faces of a U-turn will point roughly in the same direction, whereas for an S-turn, the two faces will always point roughly in opposite directions. Thus, the two modes are precisely distinguished, with $\langle T^{hd}, T^{tl} \rangle_{max} > 0.9$ defined as U-turn, and $\langle T^{hd}, T^{tl} \rangle_{max} < 0.9$ as S-turn.

Theoretical prediction of Z_c (the gray dotted line) and the result of our numerical experiment (points) are shown in Fig. 7(c). It is seen that at low Re , e.g., $Re < 2$, the prediction of Z_c precisely separates the U-turn and S-turn, which are represented by the red inverted triangles and the green dots, respectively. As Re increases, e.g., $Re = 2$ and $Re = 4$, the theoretical predicted value is slightly greater than the actual value. The over-prediction can be explained as follows. In our theoretical analysis, the calculation of hydrodynamic force is based on the resistive force theory of viscous flow. That implies that our analysis is only accurate if the Reynolds number is small. The additional inertial effect makes S-turn mode more likely to occur.

As the Reynolds number increases continuously, e.g., $Re = 8$, stable mode emerges, which is represented by a gray square as shown in the upper part of Fig. 7(c). The filaments no longer tumble with the external flow but are roughly aligned with the flow direction and form a small angle with a tiny deformation as shown in Fig. 7(b). This phenomenon is essentially caused by inertial effects, which has been explained in detail in the work of Aidun *et al.*⁴³

It is worth mentioning that we also observe that the critical flow strength between the C-buckling and the U-turn is about 858-1717, which is generally consistent with the results of Liu *et al.*¹⁷ The work of Liu *et al.*¹⁷ considered the balance between viscous, elastic, and Brownian forces, while our work considered the balance between viscous, elastic, and inertial forces. Moreover, the work of Liu *et al.*¹⁷ focuses on a limit of zero Reynolds number and applies to large molecules such as actin. Our work focuses on slightly larger filaments, such as wood fibers and nylon fibers, which undergo motion at finite Reynolds numbers.

C. Rheological property

Here, we would like to discuss the variation of the macroscopic rheology property of the dilute suspension due to different motion modes. For the suspension of filament, polymer stress can be written as⁴⁴

$$\Sigma_{ij}^{(p)} = \int_{A_0} \{ \sigma_{ik} x_j n_k - \mu (u_i n_j + u_j n_i) \} dA - \int_{V_0} \frac{\partial \sigma_{ik}}{\partial x_k} x_j dV - \int \rho u'_i u'_j dV. \quad (29)$$

Here, $\sigma_{ij} = -p\delta_{ij} + \mu \left(\frac{\partial v_i}{\partial x_j} + \frac{\partial v_j}{\partial x_i} \right)$ is the fluid stress tensor and n_i is the fiber surface normal vector. In actual statistics, first, FFT is used to calculate the period of tumbling, and then the first ten cycles are averaged. All cases in this subsection are obtained for $Re = 0.125$, and the result is general for small Reynolds numbers.

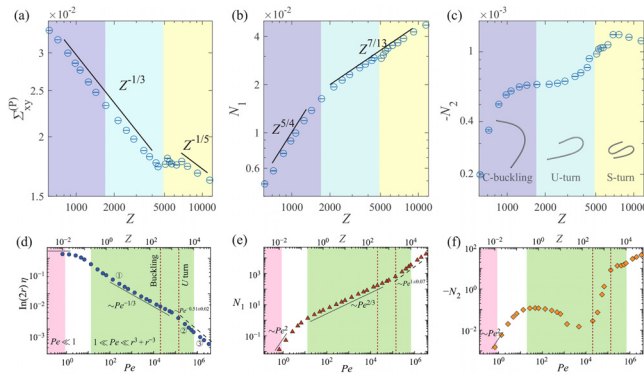


FIG. 8. (a) Polymer viscosity, (b) the first normal stress difference N_1 , (c) the second normal stress difference N_2 as functions of Z . The blue circles are numerical results, and the black solid lines are scale law of approximate fitting. (d)–(f) Polymer viscosity and normal stress difference of filament with Brownian force, regardless of fluid inertia (from Ref. 22)

The calculated relative polymer viscosity, denoted as $\Sigma_{xy}^{(p)}$, is presented in Fig. 8(a). The observed decrease in $\Sigma_{xy}^{(p)}$ indicates the shear-thinning behavior of the flexible filament solution. Notably, during the transition from C-buckling to U-turn modes, $\Sigma_{xy}^{(p)}$ demonstrates a nearly consistent scaling rate of approximately $-\frac{1}{3}$. However, a pronounced shift occurs between the U-turn and S-turn modes, resulting in a distinctive plateau in the viscosity curve. Additionally, within the S-turn phase, $\Sigma_{xy}^{(p)}$ follows an approximate power law relationship of $-\frac{1}{5}$.

For the first normal stress difference $N_1 = \Sigma_{xx}^{(p)} - \Sigma_{yy}^{(p)}$ [see Fig. 8(b)], the situation was different. There is a sharp change in the scale law from C-buckling to U-turn, but an identical scale law from U-turn to S-turn is observed. The situation of the second normal stress difference $N_2 = \Sigma_{yy}^{(p)} - \Sigma_{zz}^{(p)}$ [Fig. 8(c)] is more complicated, it is difficult to describe with scale law.

The first row of Fig. 8 presents our calculation results, while the second row displays the calculation results of Chakrabarti *et al.*²² The overall trend observed in both studies is very similar; however, due to the inclusion of Brownian forces in the model of Chakrabarti *et al.*,²² while our model incorporates inertial forces, there are notable distinctions in specific details. In the work of Chakrabarti *et al.*,²² the influence of thermal fluctuations is considered. It was discovered that rheological properties exhibit a power law relationship with flow strength across different Péclet number ranges, consistent with previous theoretical predictions.⁴⁵ The results presented by Chakrabarti *et al.*²² are visually striking. However, due to random shape fluctuations and rotational diffusion induced by thermal fluctuations, different filament motion modes can occur within different periods at the same flow strength. Consequently, it becomes challenging to determine which mode transition is responsible for the changes in rheological scaling rate or whether the series of deformation mode transitions collectively contribute.

To clarify these uncertainties, we intentionally exclude the effects of thermal fluctuations, ensuring that our filaments strictly adhere to the same motion mode within each cycle under a specific flow strength. This approach allows us to obtain less ambiguous scaling rates, enabling a clearer observation of the impact of mode transitions on the scaling rate.

The behavior of the first normal stress difference, denoted as N_1 , has been a subject of long-standing debate. In the pioneering work by Becker *et al.*,¹⁵ N_1 was observed to initially increase with the flow strength but then decrease and eventually become negative as the flow strength further increased. However, in contrast to these findings, the results presented by Chakrabarti *et al.*²² demonstrate that N_1 continues to increase with increasing flow strength. The discrepancy between these studies was attributed by Chakrabarti *et al.*²² to the perturbation of filament backbones in the simulations conducted by Becker *et al.*¹⁵

In our study, as shown in Fig. 8(b), our final results are consistent with those of.²² However, we disagree with the notion that a negative first normal stress difference (N_1) is caused by initial perturbations. Despite applying the same small initial perturbation as Becker and Shelley,¹⁵ our results show that it does not lead to a negative N_1 . Instead, we suspect that inadequate resolution of the solid grid may contribute to a misleading perception of rigidity under large deformations, as discussed by Babuvska and Rheinboldt.⁴⁶ This issue could potentially explain the negative N_1 observed in Becker *et al.*¹⁵

D. The relationship between filament deformation and polymer stress

Previous research has predominantly focused on either the microscopic deformation of filaments or the overall rheological properties of macroscopic solutions. However, studies that comprehensively illustrate the detailed connection between the two are scarce. Similar to the work of Tornberg *et al.*,⁴⁷ our strategy is that the motion and deformation of the filament lead to the creation of disturbance flow, and there exists a corresponding relationship between the disturbance flow and polymer stress. In the Stokes regime, the disturbance flow is a linear function of the tractions at the filament surface and the velocities,⁴⁸

$$\begin{aligned} \mathbf{v}(\mathbf{x}) = & -\frac{1}{8\pi\mu} \int_{\partial V} \mathbf{J}(\mathbf{x} - \mathbf{x}_0) \cdot \mathbf{t}(\mathbf{x}_0) dA_0 \\ & + \frac{1}{4\pi} \int_{\partial V} \mathbf{n}(\mathbf{x}_0) \cdot \mathbf{K}(\mathbf{x} - \mathbf{x}_0) \cdot \mathbf{v}(\mathbf{x}_0) dA_0, \end{aligned} \quad (30)$$

where $\mathbf{t} = \mathbf{n} \cdot \boldsymbol{\sigma}$ represents the component of the fluid stress tensor $\boldsymbol{\sigma}$ along the surface normal vector \mathbf{n} . \mathbf{J} and \mathbf{K} denote the Oseen tensor and its symmetric gradient,

$$J_{ij}(\mathbf{x}) = \frac{\delta_{ij}}{x} + \frac{x_i x_j}{x^3}, \quad K_{ijk}(\mathbf{x}) = \frac{1}{2} \left(\frac{\partial J_{ij}}{\partial x_k} + \frac{\partial J_{ik}}{\partial x_j} \right) = -3 \frac{x_i x_j x_k}{x^5}. \quad (31)$$

When no external forces are applied, the first-order term of Eq. (30) is consistently zero. The second-order term in the multipole expansion of Eq. (30) is expressed as⁴⁹

$$\mathbf{v}_i(\mathbf{x}) = \frac{1}{8\pi\eta_0} \left[\left(\frac{x_i \delta_{jk}}{x^3} - 3 \frac{x_i x_j x_k}{r^5} \right) S_{jk} + \varepsilon_{ijk} L_j \frac{x_k}{x^3} \right], \quad (32)$$

where S and L denote the first symmetric force moment (stresslet) and net torque (rotlet),

$$\begin{aligned} S_{ij} = & \int_{\partial V} \left[\frac{1}{2} (\sigma_{ik} x_j + \sigma_{jk} x_i) n_k - \mu (v_i n_j + v_j n_i) \right] dA, \\ L_i = & \varepsilon_{ijk} \int_{\partial V} \sigma_{jl} x_k n_l dA. \end{aligned} \quad (33)$$

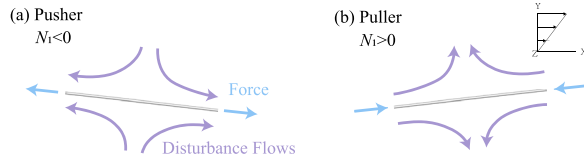


FIG. 9. (a) Filament aligned with the compression quadrant and the disturbance flow with $N_1 < 0$ is often called pusher. (b) Filament aligned with the extension quadrant and the disturbance flow with $N_1 > 0$ is often called puller. Light blue arrows represent the forces exerted by the filament on the surrounding fluid, while light purple arrows represent the disturbance flow caused by the presence of the filament.

In the absence of externally applied torque, $L_i = 0$, thereby establishing a linear relationship between stresslet and disturbance flow. As depicted in Fig. 9(a), when the rigid filament is in the compression quadrant, causing the disturbance fluid to converge from the vertical direction and push it out along the horizontal direction, resulting in $N_1 < 0$, commonly referred to as a “pusher”.^{50,51} Correspondingly, as shown in Fig. 9(b), when the rigid filament is in the extension quadrant, causing the disturbance fluid to converge from the horizontal direction and push it out along the vertical direction, leading to $N_1 > 0$, denoted as a “puller.” If we neglect the inertia terms associated with the fluctuations about the average motion, the last two terms of Eq. (29) will vanish, rendering S_{ij} and the symmetric parts of $\Sigma_{ij}^{(p)}$ fully equivalent.

To address the relationship in detail, we present the changes in polymer stress and normal stress difference over time for three different filament motion modes in Fig. 10. Before delving into each mode individually, it is important to address some common considerations. In Fig. 10, both the normal stress difference N_1 and N_2 are plotted, while the complete component of polymer stress is not. The rationale behind this omission is that throughout the cycle, the values of $\Sigma_{zz}^{(p)}$, $\Sigma_{xz}^{(p)}$, and $\Sigma_{yz}^{(p)}$ are almost zero. Recall that $N_2 = \Sigma_{yy}^{(p)} - \Sigma_{zz}^{(p)}$, and thus, the curve representing N_2 and the curve representing $\Sigma_{yy}^{(p)}$ always coincide perfectly. Similarly, since $N_1 = \Sigma_{xx}^{(p)} - \Sigma_{yy}^{(p)}$, and considering that $\Sigma_{xx}^{(p)}$ is much larger than $\Sigma_{yy}^{(p)}$, the curves of N_1 and $\Sigma_{xx}^{(p)}$, although distinguishable, are consistently very close. The three subgraphs in Fig. 10 share the same horizontal axis, and the filaments are initially positioned at rest along the flow direction and commence moving with the fluid at $t = 0$.

As shown in Fig. 10(a), under the condition of C-buckling, the filament undergoes a small “C” shape bending deformation during the tumbling process. In half a cycle, both curves of N_1 and $\Sigma_{xx}^{(p)}$ exhibit a valley and a peak at t_I and t_{III} , respectively. The corresponding filament shapes at t_I and t_{III} are depicted in the upper part of Fig. 10(a). The occurrence of these two extrema can be explained as follows. First, the maximum compression and maximum stretching of the hyperbolic flow occur in the orientations of -45° and 45° , respectively. Therefore, for a rigid filament, suppose the angle between the filament axis and the incoming flow is ϕ , then the strain rate of the fluid along the filament axis is proportional to $\sin(2\phi)$. In the global coordinate system, the x -component of the polymer stress $\Sigma_{xx}^{(p)}$ should be proportional to $\sin(2\phi) \cos(\phi)$, and this function reaches a minimum (maximum) value at $\phi = -35^\circ$ ($\phi = 35^\circ$) [see upper part of Fig. 10(a)]. Similarly, the y -component of the polymer stress $\Sigma_{yy}^{(p)}$ is proportional

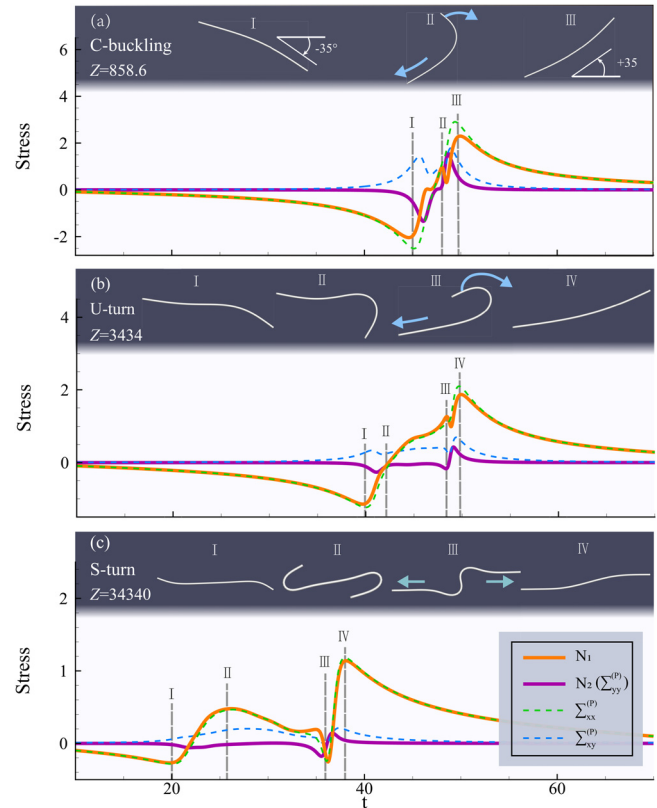


FIG. 10. The relationship of polymer stress and normal stress difference with time in the case of (a) C-buckling, (b) U-turn, and (c) S-turn during half a cycle. Images depicting the instantaneous motion at time points t_I , t_{II} , t_{III} , and t_{IV} are displayed in the upper portion of panels (a)–(c). The curves representing N_2 and $\Sigma_{yy}^{(p)}$ always coincide.

to $\sin(2\phi) \sin(\phi)$, and it reaches a minimum (maximum) value at $\phi = -55^\circ$ ($\phi = 55^\circ$). Although the above analysis is based on the rigid filament, the variation trend is still applicable to the filament with small deformation. The minor difference is that the flexible filament will store elastic energy when it is buckling at t_I and release elastic energy when it is recovering at t_{II} . At the moment of t_{II} , the upper portion of the filament stroke toward the right [see the light blue arrow in Fig. 10(a-II)], and correspondingly, the remaining part of the filament accelerates toward the left, moving like a pusher, and corresponds to a small decrease in the N_1 curve at t_{II} . On the whole, it is the filament’s flexibility that leads to the integral of N_1 over one period being non-zero, and the filament solution exhibits viscoelasticity.

The U-turn mode shown in Fig. 10(b) is broadly similar to the C-buckling described above. Because the filament is more flexible in this case, the buckling occurs earlier (at $\phi \approx -13^\circ$), and the polymer stress at buckling (t_I) is also smaller than that at C-buckling. The more essential difference is that the filaments exhibit tank-treading motions (t_{II} to t_{III}) during U-turn, both $\Sigma_{xx}^{(p)}$ and $\Sigma_{yy}^{(p)}$ show a positive slowly rising plateau, and $\Sigma_{yy}^{(p)}$ exhibits a near-zero plateau. When the tank-treading motions end (t_{III}), the stored elasticity within the flexible filament is suddenly released, a quick stroke [see the light blue arrow in

Fig. 10(b-III)] occurs at the right end of the filament, while the remaining part of the filament accelerates toward the left. The filament acts as a pusher, and the N_1 curve descends. After the tank-treading is completely finished, similar to C-buckling, $\Sigma_{xx}^{(p)}$ and $\Sigma_{xy}^{(p)}$ rise sharply and reach their maximum value (t_{IV}).

The S-turn mode shown in Fig. 10(c) is very unique, which is mainly reflected in the fact that both ends of the filament go through tank-treading motions (t_{II} - t_{III}) at the same time. Compared to U-turn, the S-turn has a longer duration of tank-treading, which lasts about 0.1 period. As shown in the lower part of Fig. 10(c), both $\Sigma_{xx}^{(p)}$ and $\Sigma_{xy}^{(p)}$ experienced a long positive but slowly declining plateau and $\Sigma_{yy}^{(p)}$ exhibits a near-zero plateau (from t_{II} to t_{III}). The decrease in $\Sigma_{xx}^{(p)}$ and $\Sigma_{xy}^{(p)}$ can be attributed to the fact that as tank-treading progresses, the inclination angle of the straight section of the filament gradually decreases, resulting in less stretching by the flow field. As the tank-treading motion approaches its end, the two bending regions of the filament come closer together and eventually merge, leading to the release of stored elasticity within the filament. When the two bending regions of the filament come into contact, the internal elastic forces push the right half of the filament accelerates to the right while the left half accelerates to the left [see the light blue arrow in Fig. 10(c-III)]. The filament acts as a pusher, and corresponding to a decrease in N_1 . In general, the magnitude of N_1 in the S-turn mode is much smaller than in the U-turn mode. However, due to the longer duration of tank-treading and the shorter tumbling period in the S-turn mode, the average value of N_1 in the S-turn mode can even be larger than that in the U-turn mode.

From the above discussion, we find that there is an inseparable relationship between $\Sigma_{xx}^{(p)}$ and filament shape. In order to quantitatively analyze the internal relationship between the two, we introduce the gyration tensor,^{11,17}

$$G_{\xi\eta} = \sum_{i=1}^N (s_{\xi}(i, t) - \bar{s}_{\xi}(t))(s_{\eta}(i, t) - \bar{s}_{\eta}(t)) / N, \quad (34)$$

where $s_{\xi}(i, t)$ is the position of the i th node at time t , $\bar{s}_{\xi}(t)$ is the average position of the filament at time t , and N is the total number of solid nodes. In the polymer stress tensor, the normal stress in the x -direction $\Sigma_{xx}^{(p)}$ is absolutely dominant. In order to better understand the complex changes of $\Sigma_{xx}^{(p)}$, we further define the generalized strain of filament in the x -direction,

$$E_{\xi\eta} = \frac{\overline{G_{\xi\eta}} - G_{\xi\eta}^0}{G_{\xi\eta}^0}, \quad (35)$$

where $\overline{G_{\xi\eta}}$ is the periodic average of the gyration tensor, and $G_{\xi\eta}^0$ is the periodic average of the gyration tensor of rigid filament. In this paper, we use the example of $Z = 5$ to represent a rigid filament. As shown in Fig. 11, we observe that the generalized strain in the x -direction is directly proportional to the polymer stress, just like Hooke's law. We find that the points near the lower right corner slightly deviate from the linear relationship, which may be mainly due to the small generalized strain corresponding to these points, so the error introduced by the approximate calculation of $G_{\xi\eta}^0$ is revealed. This linear relationship means that even though the deformation of the different modes is

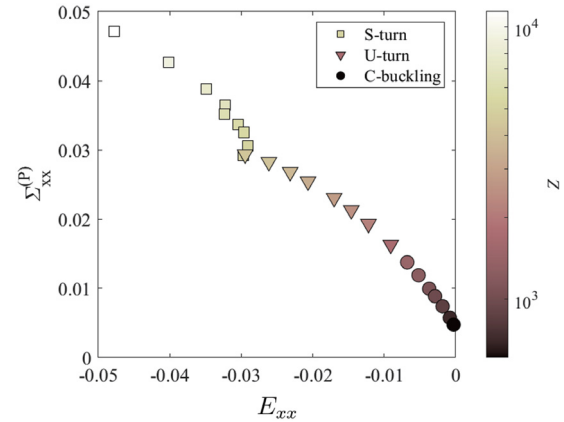


FIG. 11. Relationship between the filament's x -direction deformation and the x -direction normal polymer stress, with different colors representing different flow strengths.

complex, the time-varying curve of the resulting polymer stress is different. We still found some statistics that unite them. It is worth noting that for filaments considering thermal fluctuations, the linear relationship may not be observed after time averaging due to the existence of rotational diffusion. Therefore, this observed linear relationship may only apply to flexible filaments with large characteristic length (on the order of 0.1 mm, for example, for pulp fibers) in flows with relatively high shear rates.

IV. CONCLUDING REMARKS

We present a comprehensive investigation of the behavior of a non-Brownian flexible filament in three dimensions under low Reynolds number shear flow. Our study includes the development of a theoretical model for the S-turn mode and a thorough theoretical analysis to determine the critical flow strength needed for the transition from U-turn to S-turn mode, which is estimated to be $Z_c = 4900$. We also conducted numerical simulations, which identified four distinct motion modes. The phase diagram of the motion modes in the (Re, Z) -plane is presented, and our simulation results confirmed the theoretical prediction of Z_c . Moreover, our study revealed a direct association between the filament's motion modes and the scaling transition of solution rheological properties. We provided a detailed description of the relationship between the deformation of the filament and polymer stress over time, as well as highlighted significant differences in polymer stress curves under different modes. Interestingly, we observe an overall linear relationship between time-averaged polymer stress and the generalized strain.

ACKNOWLEDGMENTS

We wish to acknowledge the support of the National Science Foundation of China (NSFC) (Grant Nos. 11772326 and 11972342). The authors thank Dr. Yanan Liu for fruitful discussions and suggestions. In addition, this research is supported by the Supercomputing Center of the USTC.

AUTHOR DECLARATIONS

Conflict of Interest

The authors have no conflicts to disclose.

Author Contributions

Yetao Lu: Conceptualization (supporting); Data curation (lead); Formal analysis (lead); Funding acquisition (supporting); Investigation (lead); Methodology (lead); Project administration (supporting); Resources (supporting); Software (supporting); Supervision (supporting); Validation (lead); Visualization (lead); Writing – original draft (lead); Writing – review & editing (supporting). **Haibo Huang:** Conceptualization (lead); Data curation (supporting); Formal analysis (supporting); Funding acquisition (lead); Investigation (supporting); Methodology (supporting); Project administration (lead); Resources (lead); Software (lead); Supervision (lead); Validation (supporting); Visualization (supporting); Writing – original draft (supporting); Writing – review & editing (lead).

DATA AVAILABILITY

The data that support the findings of this study are available from the corresponding author upon reasonable request.

REFERENCES

- ¹J. Deng, X. R. Mao, and L. Brandt, “Symmetry breaking of tail-clamped filaments in stokes flow,” *Phys. Rev. Lett.* **126**, 124501 (2021).
- ²E. Lauga, “Bacterial hydrodynamics,” *Annu. Rev. Fluid Mech.* **48**, 105–130 (2016).
- ³M. J. Shelley, “The dynamics of microtubule/motor-protein assemblies in biology and physics,” *Annu. Rev. Fluid Mech.* **48**, 487–506 (2016).
- ⁴J. S. Hur, E. S. G. Shaqfeh, and R. G. Larson, “Brownian dynamics simulations of single DNA molecules in shear flow,” *J. Rheol.* **44**, 713–742 (2000).
- ⁵F. Lundell, L. D. Soderberg, and P. H. Alfredsson, “Fluid mechanics of paper-making,” *Annu. Rev. Fluid Mech.* **43**, 195–217 (2011).
- ⁶G. B. Jeffery, “The motion of ellipsoidal particles immersed in a viscous fluid,” *Proc. R. Soc. London, Ser. A* **102**, 161–179 (1922).
- ⁷R. G. Cox, “The motion of long slender bodies in a viscous fluid. Part 2. Shear flow,” *J. Fluid Mech.* **45**, 625–657 (1971).
- ⁸L. Leal, “The slow motion of slender rod-like particles in a second-order fluid,” *J. Fluid Mech.* **69**, 305–337 (1975).
- ⁹G. Subramanian and D. L. Koch, “Inertial effects on fibre motion in simple shear flow,” *J. Fluid Mech.* **535**, 383–414 (2005).
- ¹⁰E.-J. Ding and C. K. Aidun, “The dynamics and scaling law for particles suspended in shear flow with inertia,” *J. Fluid Mech.* **423**, 317–344 (2000).
- ¹¹C. Xu, X. C. Liu, K. Liu, Y. F. Xiong, and H. B. Huang, “A free flexible flap in channel flow,” *J. Fluid Mech.* **941**, A12 (2022).
- ¹²O. du Roure, A. Lindner, E. N. Nazockdast, and M. J. Shelley, “Dynamics of flexible fibers in viscous flows and fluids,” *Annu. Rev. Fluid Mech.* **51**, 539–572 (2019).
- ¹³A. Salinas and J. F. T. Pittman, “Bending and breaking fibers in sheared suspensions,” *Polym. Eng. Sci.* **21**, 23–31 (1981).
- ¹⁴O. L. Forgacs and S. G. Mason, “Particle motions in sheared suspensions IX. Spin and deformation of threadlike particles,” *J. Colloid Sci.* **14**, 457–472 (1958).
- ¹⁵L. E. Becker and M. J. Shelley, “Instability of elastic filaments in shear flow yields first-normal-stress differences,” *Phys. Rev. Lett.* **87**, 198301 (2001).
- ¹⁶M. Harasim, B. Wunderlich, O. Peleg, M. Kroger, and A. R. Bausch, “Direct observation of the dynamics of semiflexible polymers in shear flow,” *Phys. Rev. Lett.* **110**, 108302 (2013).
- ¹⁷Y. A. Liu, B. Chakrabarti, D. Saintillan, A. Lindner, and O. du Roure, “Morphological transitions of elastic filaments in shear flow,” *Proc. Natl. Acad. Sci. U. S. A.* **115**, 9438–9443 (2018).
- ¹⁸H. K. S. Goto and H. Nagazono, “The flow behavior of fiber suspensions in Newtonian fluids and polymer solutions. I. Mechanical properties,” *Rheol. Acta.* **25**, 119–129 (1986).
- ¹⁹K. Weissenberg, “A continuum theory of rheological phenomena,” *Nature* **159**, 310–311 (1947).
- ²⁰K. P. Chen and Y. Zhang, “Stability of the interface in co-extrusion flow of two viscoelastic fluids through a pipe,” *J. Fluid Mech.* **247**, 489–502 (1993).
- ²¹É. Couturier, F. Boyer, O. Pouliquen, and É. Guazzelli, “Suspensions in a tilted trough: Second normal stress difference,” *J. Fluid Mech.* **686**, 26–39 (2011).
- ²²B. Chakrabarti, Y. Liu, O. du Roure, A. Lindner, and D. Saintillan, “Signatures of elastoviscous buckling in the dilute rheology of stiff polymers,” *J. Fluid Mech.* **919**, A12 (2021).
- ²³R. G. Larson, *The Structure and Rheology of Complex Fluids* (OUP USA, 1999).
- ²⁴H. Janeschitz-Kriegl, *Polymer Melt Rheology and Flow Birefringence* (Springer Science & Business Media, 1983), Vol. 6.
- ²⁵W. Kuhn and F. Grün, “Beziehungen zwischen elastischen konstanten und dehnungsdoppelbrechung hochelastischer stoffe,” *Kolloid-Z.* **101**, 248–271 (1942).
- ²⁶L. G. Treloar, *The Physics of Rubber elasticity* (OUP Oxford, 1975).
- ²⁷J. B. Keller and S. I. Rubinow, “Slender-body theory for slow viscous flow,” *J. Fluid Mech.* **75**, 705–714 (1976).
- ²⁸J. F. Doyle, *Nonlinear Analysis of Thin-Walled Structures: Statics, Dynamics, and Stability* (Springer Science & Business Media, 2001).
- ²⁹A. A. Banaei, M. E. Rosti, and L. Brandt, “Numerical study of filament suspensions at finite inertia,” *J. Fluid Mech.* **882**, A5 (2020).
- ³⁰T. Krüger, H. Kusumaatmaja, A. Kuzmin, O. Shardt, G. Silva, and E. M. Viggien, *The Lattice Boltzmann Method* (Springer, 2017), Vol. 10, pp. 407–430.
- ³¹J. S. Wu and C. K. Aidun, “A method for direct simulation of flexible fiber suspensions using lattice Boltzmann equation with external boundary force,” *Int. J. Multiphase Flow* **36**, 202–209 (2010).
- ³²M. Do-Quang, G. Amberg, G. Brethouwer, and A. V. Johansson, “Simulation of finite-size fibers in turbulent channel flows,” *Phys. Rev. E* **89**, 013006 (2014).
- ³³D. Goldstein, R. Handler, and L. Sirovich, “Modeling a no-slip flow boundary with an external force field,” *J. Comput. Phys.* **105**, 354–366 (1993).
- ³⁴X. L. Yang, X. Zhang, Z. L. Li, and G. W. He, “A smoothing technique for discrete delta functions with application to immersed boundary method in moving boundary simulations,” *J. Comput. Phys.* **228**, 7821–7836 (2009).
- ³⁵W. Kim, I. Lee, and H. Choi, “A weak-coupling immersed boundary method for fluid-structure interaction with low density ratio of solid to fluid,” *J. Comput. Phys.* **359**, 296–311 (2018).
- ³⁶W.-X. Huang, S. J. Shin, and H. J. Sung, “Simulation of flexible filaments in a uniform flow by the immersed boundary method,” *J. Comput. Phys.* **226**, 2206–2228 (2007).
- ³⁷B. Trevelyan and S. G. Mason, “Particle motions in sheared suspensions. I. Rotations,” *J. Colloid Sci.* **6**, 354–367 (1951).
- ³⁸C. Zhang, H. Huang, and X.-Y. Lu, “Effect of trailing-edge shape on the self-propulsive performance of heaving flexible plates,” *J. Fluid Mech.* **887**, A7 (2020).
- ³⁹J. Gray and G. Hancock, “The propulsion of sea-urchin spermatozoa,” *J. Exp. Biol.* **32**, 802–814 (1955).
- ⁴⁰W. Zhao and H. Lee, “Spontaneous breaking of topological symmetry,” *Phys. Rev. Lett.* **68**, 1451 (1992).
- ⁴¹S. Midorikawa, “Symmetry restoration of the electroweak interactions,” *Phys. Rev. D* **22**, 2045 (1980).
- ⁴²T. Nishi, K. Itahashi, D. Ahn, G. P. Berg, M. Dozono, D. Etoh, H. Fujioka, N. Fukuda, N. Fukunishi, H. Geissel *et al.*, “Chiral symmetry restoration at high matter density observed in pionic atoms,” *Nat. Phys.* **19**, 788–793 (2023).
- ⁴³C. K. Aidun, Y. Lu, and E.-J. Ding, “Direct analysis of particulate suspensions with inertia using the discrete Boltzmann equation,” *J. Fluid Mech.* **373**, 287–311 (1998).
- ⁴⁴G. K. Batchelor, “The stress system in a suspension of force-free particles,” *J. Fluid Mech.* **41**, 545–570 (1969).
- ⁴⁵E. J. Hinch, “The distortion of a flexible inextensible thread in a shearing flow,” *J. Fluid Mech.* **74**, 317–333 (1975).

- ⁴⁶I. Babuška and W. C. Rheinboldt, “A-posteriori error estimates for the finite element method,” *Numer. Meth. Eng.* **12**, 1597–1615 (1978).
- ⁴⁷A.-K. Tornberg and M. J. Shelley, “Simulating the dynamics and interactions of flexible fibers in stokes flows,” *J. Comput. Phys.* **196**, 8–40 (2004).
- ⁴⁸C. Pozrikidis, *Boundary Integral and Singularity Methods for Linearized Viscous Flow* (Cambridge university Press, 1992).
- ⁴⁹S. Kim and S. J. Karrila, *Microhydrodynamics: Principles and Selected Applications* (Courier Corporation, 2013).
- ⁵⁰M. J. Lighthill, “On the squirming motion of nearly spherical deformable bodies through liquids at very small Reynolds numbers,” *Comm. Pure Appl. Math.* **5**, 109–118 (1952).
- ⁵¹D. Saintillan, “Rheology of active fluids,” *Annu. Rev. Fluid Mech.* **50**, 563–592 (2018).